Appl Phys B (2011) 102: 279–291
DOI 10.1007/s00340-010-4002-1

Applied Physics B
Lasers and Optics

VCSEL based Faraday rotation spectroscopy with a modulated and static magnetic field for trace molecular oxygen detection

S.G. So · E. Jeng · G. Wysocki

Received: 13 January 2010 / Revised version: 6 March 2010 / Published online: 17 April 2010

Abstract Faraday Rotation Spectroscopy (FRS) is a useful technique for quantification of paramagnetic trace gases with significantly higher sensitivity when compared to direct absorption techniques. Our prototype system based on the openPHOTONS sensor core measures the concentration of molecular oxygen (O_2) in the A band using a 763-nm vertical cavity surface emitting laser. We provide detailed analysis of two measurement methods based on FRS using the same sensor configuration: one with a modulated magnetic field, and one with a static magnetic field in combination with wavelength modulation. Our spectra signal-to-noise ratios agree well with our simulations via modeling of the FRS signal. For alternating magnetic field, we achieve an equivalent minimum detectable absorption (MDA) of $8.86 \times 10^{-7}/\mathrm{Hz}^{\frac{1}{2}}$ resulting in a minimum detection limit of 30 ppmv·m/$\mathrm{Hz}^{\frac{1}{2}}$ of O_2, limited by detector noise and laser noise. For the same system configuration in the static field case, parasitic etalon fringes limited the MDA to $4.8 \times 10^{-6}/\mathrm{Hz}^{\frac{1}{2}}$. In both cases, we describe methods to improve signal-to-noise ratio based on our data and models.

1 Introduction

Faraday Rotation Spectroscopy (FRS) exploits magnetic circular birefringence (MCB) observed in the vicinity of Zeeman split absorption lines and provides enhanced detection of paramagnetic molecules. The MCB induced by the magnetic field along the direction of optical beam propagation causes rotation of the polarization axis of linearly polarized light. Due to efficient suppression of the laser noise [1], FRS can achieve high sensitivities within short optical paths, which is of particular interest in the development of compact, low power instrumentation measuring trace concentrations of paramagnetic molecular species. The common approach for generating FRS signals is based on an alternating magnetic field (AC-field), which modulates the Zeeman splitting of the absorption lines. This produces varying MCB and results in modulated polarization rotation of the transmitted light. After the gas cell, a second polarizer (analyzer) transforms this polarization rotation into modulation of the intensity of light reaching the detector, which is demodulated using a phase-sensitive lock-in amplifier. An alternative FRS detection scheme uses a static magnetic field (DC-field) and laser wavelength modulation to effectively vary the MCB. For the DC-field method, a similar detection scheme based on a polarization analyzer and a lock-in amplifier provides FRS signal demodulation.

Our motivation for this work is to develop low-power, low-cost, handheld trace gas sensors for environmental, medical, and security applications. FRS can provide more compact, robust sensors which are more easily and reliably field deployable than other instrumentation which senses O_2, NOx, and free radical species with high sensitivity and specificity. The DC method has potential to offer a significant reduction of total power consumption by applying permanent magnets in place of electromagnetic field generation required in the AC-field approach. We will describe the ultimate sensitivity and trade-offs in both methods by using the same sensor architecture with both AC- and DC-detection schemes.

S.G. So (✉) · E. Jeng · G. Wysocki
Electrical Engineering Department, Princeton University,
Engineering Quad, Princeton, NJ, USA
e-mail: sso@princeton.edu
Fax: +1-609-2583745

G. Wysocki
e-mail: gwysocki@princeton.edu

A secondary goal of this work is to provide a rigorous test of the openPHOTONS (PHOTOnic Networked Sensors) core system [2]. This core is an ultra-low-power laser spectroscopic sensor control system, capable of use in a variety of laser sensing techniques. By integrating a flexible combination of sensor control/measurement electronics and firmware, the openPHOTONS core provides a common platform for a variety of optical sensors. Since the measured signals in FRS are extremely small and strongly dependent on overall noise characteristics of the detection and laser systems, this sensing technique exercises the limits of the core system control, acquisition, and processing methods. Primarily, we are implementing these sensors in order to enable handheld wearable exposure monitors for health and industrial applications, and for wireless sensor network applications. These sensors require (1) handheld compact size, (2) low power consumption, (3) robustness, (4) autonomy, (5) high sensitivity, and (6) specificity.

In this work, we use FRS techniques to sense molecular oxygen (a relatively stable paramagnetic molecule). We implement oxygen in order to target an environmental application which requires high specificity to oxygen (no cross-sensitivity issues, e.g., dependence on humidity levels). Ultimately, the sensor sensitivity and specificity must provide the capability of real-time measurement of biotic respiration rates (CO_2–O_2 exchange at single ppmv level) in the field in short time scales (<0.1 seconds). Standard oxygen sensors [3, 4] include electrochemical oxygen sensors (which have a short working life, should not be duty cycled due to thermal stress issues in the case of Zirconium Oxide, and may have slow response), paramagnetic magnetodynamic oxygen sensors (sensitive to vibration and/or position, cross sensitivity to NOx and other paramagnetic molecules), and infrared direct absorption laser spectroscopy (which typically require a long optical path for high sensitivity, which in demanding applications can be sensitive to temperature and vibration). Although well established and commercially available, these technologies are not able to provide the required specifications for O_2 sensing at low ppmv levels in short time scales with low power dissipation. The target sensor should also be able to operate maintenance free in the field on long time scales (months to years), yet still provide an ultra-compact form factor, low power operation, and relatively low cost. Other paramagnetic molecules of interest in both atmospheric and medical trace gas sensing are NO, NO_2, and free radicals such as ·OH or ·HO_2, which may be addressed using the same FRS sensor platform.

2 Background

2.1 Selection of O_2 transition

Paramagnetic molecules possess a permanent magnetic dipole moment due to unpaired electrons in the molecular orbitals. Molecular orbital theory shows two unpaired electrons in the O_2 $2p\ \pi^*$ orbitals. For target transitions ($^PP(J)$ and $^PQ(J)$), the upper state is a singlet state, and there is no electron spin magnetic moment. The contribution of the nuclear spin magnetic moment is negligible, so there is no splitting of the upper state. The ground state energy levels are Zeeman split under the influence of a magnetic field into two components selectively affecting left- and right-hand circularly polarized (LHCP and RHCP) light. Interaction of LHCP and RHCP light with the Zeeman split transitions results in MCB around the absorption lines. This results in Faraday rotation of linear input polarization, and the magnitude of the polarization rotation is related to the concentration of the target molecules and the optical path through the sample.

The spin coupling and angular momentum coupling in oxygen are approximately given by Hund's case (b) [5]. The g factor follows the relationship for Hund's case (b):

$$\frac{g}{g_s} = \frac{J(J+1) + S(S+1) - N(N+1)}{2J(J+1)} \tag{1}$$

where g_s is electron spin g-factor ($g_s = -2.002$), J is the total angular momentum quantum number excluding nuclear spin, S is the angular momentum number of electron spins, and N is the rotational angular momentum quantum number. Since the g-factor is higher for low J-numbers, the low J transitions exhibit much stronger FRS signals for low magnetic fields. Thus, in this work we target the $^PP_1(1)$ ($J = 1$) line at 13 118.04 cm^{-1} wavenumbers with $g = 1.0011$ to perform evaluations of the AC and DC approaches for FRS sensing.

2.2 AC and DC magnetic field FRS

In the AC magnetic field case, the field periodically alternates the Zeeman splitting of the RHCP and LHCP transition components symmetrically around the central frequency of the transition (assuming linear Zeeman effect for relatively low magnetic field intensities). The laser operates in continuous wave (cw), and by performing a slow scan of the laser frequency, the alternating polarization rotation signal can be recorded as a function of optical frequency. Demodulation is performed using lock-in detection at the fundamental frequency of the magnetic field modulation. The first harmonic (1f) signal is proportional to the difference in the molecular dispersion spectra for RHCP and LHCP (shown as Δn in Fig. 1b). Since the magnetic field changes in a sinusoidal fashion between $-B$ and $+B$, the peak amplitude of the signal shown in Fig. 1c is proportional to the difference in the two Δn, obtained at the two extremes of B-field. Since the laser frequency is not modulated, the FRS signal in the AC method results only from the modulation of

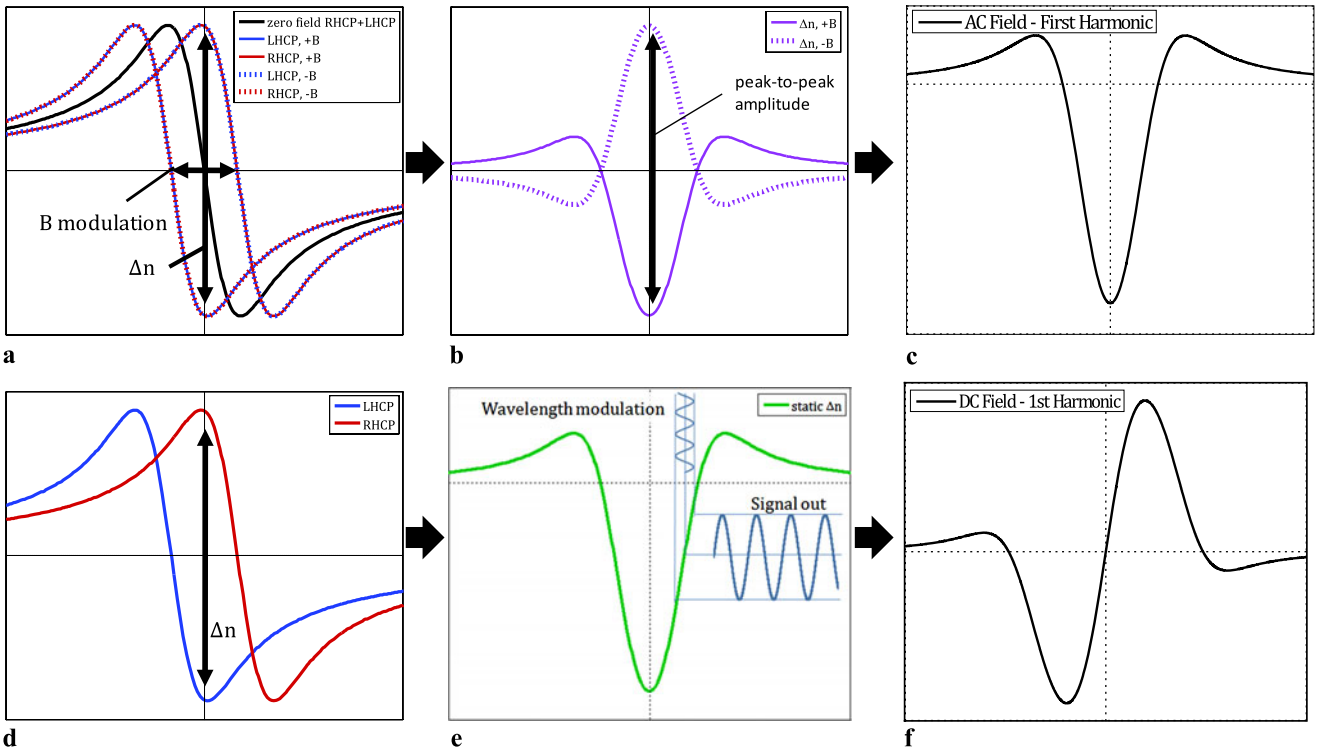

Fig. 1 *Top*: Simulations of an AC magnetic FRS signal with alternating splitting at the full width of the absorption line. **a** Shows dispersion profiles for the LHCP and the RHCP component at zero B-field and at two extremes of B-field modulation ($-B$ and $+B$). The polarization rotation at a moment in time is proportional to the difference in dispersion profiles shown as Δn in (**b**). The final demodulated FRS signal peak amplitude shown in (**c**) is proportional to a difference in Δn obtained at two extremes of B-field modulation. *Bottom*: Simulation of a DC magnetic FRS signal with a static splitting and wavelength modulation. **d** Shows dispersion profiles for the LHCP and the RHCP component at static B-field. The polarization rotation is proportional to the difference in dispersion profiles shown as Δn in (**e**). The final lock-in detected signal is a result of wavelength modulation of the laser source as shown in (**e**) and approximately resembles the first derivative of the Δn spectrum when demodulated at the first harmonic

the spectral properties of the sample and thus is less susceptible to optical interference effects (i.e., etalon fringes). The main noise sources in the AC method are the detection system noise and laser noise, which determine the sensitivity of the measurement. Another important and often underestimated source of noise and long-term drift is electromagnetic interference (EMI). The high-current AC circuit for magnetic field generation emits EM fields, and the sensor subsystems (both detection system or laser source) acquire the interfering signals at the modulation frequency through unintentional circuit loops. While the EMI due to the pickup in the detection system ideally results in a constant offset in the demodulated signal (which can be removed as long as it is stable in time), similar pick-up in the laser source circuitry results in modulation of laser current which affects both the intensity and the wavelength of emitted radiation and causes more complicated and difficult to suppress noise structure. The EMI related noise usually deteriorates the long-term stability of the system [6].

In the DC field case, the magnetic field and resulting Zeeman splitting is static. At each optical frequency, the Faraday rotation angle proportionally changes with the difference in RHCP and LHCP dispersion spectra (see Fig. 1, bottom). The applied modulation of the laser radiation wavelength produces modulation of the detected polarization state (shown in Fig. 1e). Similar to standard wavelength modulation techniques, demodulation at different harmonics of the fundamental frequency provides various derivatives of the static Faraday rotation spectrum (1f detection is demonstrated in Figs. 1e and f). Adjusting the modulation depth to the shape of the spectral feature provides optimization of signal generation (i.e., laser wavelength modulation depth approximately matched to the largest trough-to-peak of the signal will maximize first-harmonic detection magnitude, while matching the largest trough-to-peak-to-trough of the signal will maximize second-harmonic detection magnitude). The main limitation in DC field based FRS is vulnerability to optical fringing and other spectral interferences. Due to the presence of frequency varying spectral envelopes (etalons, absorption features), the modulation of the laser frequency translates into amplitude modulation of the light intensity received by the detector. The lock-in amplifier detects this amplitude modulation at the various harmonics of the excitation signal. Although this is an important limita-

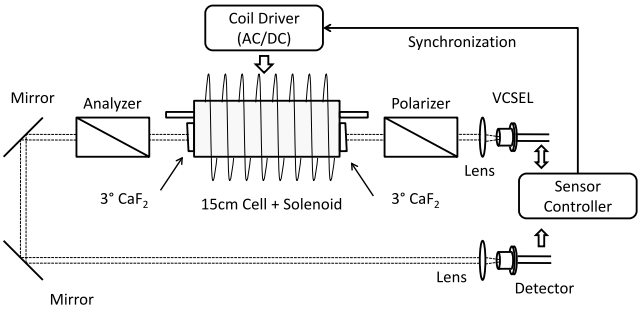

Fig. 2 Optical block diagram of the FRS system

tion of the ultimate sensitivity using the DC field, FRS can still provide performance that is superior to most of the sensing systems based on direct absorption and wavelength modulation spectroscopy.

3 Experimental methods

3.1 System configuration

The experimental setup used in this work is shown in Fig. 2. The developed system can implement both the AC and DC field FRS detection which allows direct comparison of the techniques.

The laser output of a vertical cavity surface emitting laser (VCSEL) operating at 764 nm was collimated by an ECO-550 glass aspheric lens (focal length $f = 6.24$ mm) with 600–1050 nm antireflection coating. The collimated beam then passes through the following optical system components: (1) a polarizer for improvement of the polarization purity, (2) the gas cell, (3) a second polarizer (analyzer), (4) two beam steering metallic mirrors (bare gold coating), and (5) a second $f = 6.24$ mm lens focusing the beam on the detector (Thorlabs FDS010 Si PIN diode with 1-mm diameter and responsivity of $\sim$0.42 A/W at 762 nm).

The laser in this work was from Avalon Photonics in a TO5 package with an integrated Peltier thermoelectric cooler (TEC) and thermistor. It was driven with 6 mA of bias current and required 2.25 V of compliance voltage, producing approximately 300 µW of optical power at -15°C. The laser had a pre-defined and stable axis of polarization enabling the use of these polarization-based laser spectroscopy techniques (VCSELs are known to operate with random and fluctuating polarization if a dedicated polarizing element is not incorporated in the laser chip).

The glass sample gas cell with 3°-wedged CaF_2 windows for fringe suppression was enclosed within a solenoid coil used for axial magnetic field generation. The coil was a Sargent-Welch CP72700-02 air core solenoid with 1.9 Ω of DCR (direct current resistance) and 8 mH inductance. We created a resonant series-*LC* circuit with a magnetic solenoid coil at 1.07 kHz with a 3-µF capacitor. An audio power amplifier (QSC RMX850) drives the circuit for AC-field generation, or a DC power supply produces DC-fields. We measured the AC and DC magnetic fields with a Lakeshore Model 410 Gaussmeter. The homogeneity of the magnetic field was within 20% over the length of the coil, with maximum field in the center of the gas cell.

Glan Thompson calcite polarizers from Thorlabs (GTH10M) were used as the polarizer and the analyzer. Without the gas cell between the pair, we measured 6.6×10^{-6} extinction ratio which was in agreement with the specifications. After inserting the cell, the maximum extinction ratio deteriorated, which might be a combination of effects due to birefringence of the window material and Fresnel reflections at the interface between the wedged windows and the air/sample gas. To minimize this effect we performed optimization of the cell wedge orientation with respect to the input polarization by axially rotating the cell and performing extinction ratio measurements at regularly spaced angles. The optimum position provides an extinction ratio of $\xi = 7.7 \times 10^{-5}$, compared to $\xi = 5 \times 10^{-4}$ extinction observed at a nonoptimal angle. All experiments employ the cell in the optimum position.

The system control, data acquisition, and processing were performed using the openPHOTONS core systems [2], described in [7], with customization for FRS detection.

3.2 openPHOTONS sensor core

The openPHOTONS sensor core is a comprehensive sensor platform capable of implementing a variety of laser sensing techniques including direct absorption spectroscopy, WMS, photoacoustic sensing, and FRS (presented in this work).

The board electronics are powered by a single input power supply rail of 3.3–6 V, enabling single-cell lithium-ion battery-powered operation of the entire sensor control and acquisition electronics. The external amplifier used for the AC case amplified a synthesized sine wave output from the board to drive the solenoid magnetic coil. In the DC field case, the same sine wave is used for laser wavelength modulation.

We implemented a preamplifier based on a transimpedance amplifier with feedback resistor of 1 MΩ to capture the photodetector signal. The output of the preamplifier was AC coupled into a secondary amplifier stage providing 241× gain. The microcontroller then digitizes the signal for analysis by digital lock-in detection. The board generates two digital local oscillators at arbitrary phase and harmonic for multiplication with the raw ADC value. A digital low pass filter removes the higher harmonics after the digital mixing, while restricting the detection bandwidth to an experimental 0.54 Hz (measured via 10–90% rise time from a step input).

The lock-in output, along with other sensor parameters, streams over either USB or IEEE 802.15.4 Zigbee radio, which can then be logged in a personal computer using a LabVIEW user interface. Total power consumption of the laser and control/acquisition/processing systems was ∼0.3 W when operating the laser at a temperature near 25°C and about 1 W when cooling to −15°C.

4 Results

4.1 AC field

4.1.1 System optimization

A complete noise analysis for the AC system allows us to determine the optimum operating conditions and sensitivity of the FRS sensor platform. For small analyzer offset angles α (measured from the fully crossed position of the analyzer), the signal-to-noise ratio of an FRS system [6] can be described as

$$\begin{aligned}\mathrm{SNR} &= \frac{S}{N} \\ &= \frac{a\cdot\alpha\cdot P_0}{\sqrt{b^2 + c^2\cdot P_0\cdot(\alpha^2+\xi) + d^2\cdot P_0^2\cdot(\alpha^2+\xi)^2}} \\ &= \frac{A\cdot\alpha}{\sqrt{B^2 + C^2\cdot(\alpha^2+\xi) + D^2\cdot(\alpha^2+\xi)}} \end{aligned} \tag{2}$$

where a is proportional to the Faraday rotation signal, b is the detection system noise, $c\cdot\sqrt{P_0}\sqrt{\alpha^2+\xi}$ is quantum noise generated in the detector, and $d\cdot P_0(\alpha^2+\xi)$ is the laser noise reaching the detector. Parameters A, B, C, and D are expressed in our custom digital detection system units and are used in further analysis and fitting of the measured data.

We calibrated the system experimentally by measuring a conversion factor from the custom digital detection system units to the actual optical power units. The total transfer function between the power incident on the detector and the values generated by the digital lock-in amplifier includes the responsivity of the detector, gains of the analog systems, and lock-in amplifier gain. For our system, the transfer function is $H \approx 1.6\times10^{15}$ [digital detection system units/W]. The total noise is a function of the analyzer angle. Since different order effects (with respect to angle) produce each noise component (B, C, D), we fit each component out of the experimental data using the expression in the denominator of (2). It is not possible to directly distinguish different sources of noise in the detection system, and thus B includes the detector noise, analog front end noise and distortion, and acquisition noise and distortion. Similarly, if the shot noise is small compared to detection system noise and/or laser noise, the fit of C from the measurement data is not reliable. Thus, we infer the shot noise generated in the detector (parameter C) using the responsivity of the detector, the photon energy, the extinction ratio, and the laser power.

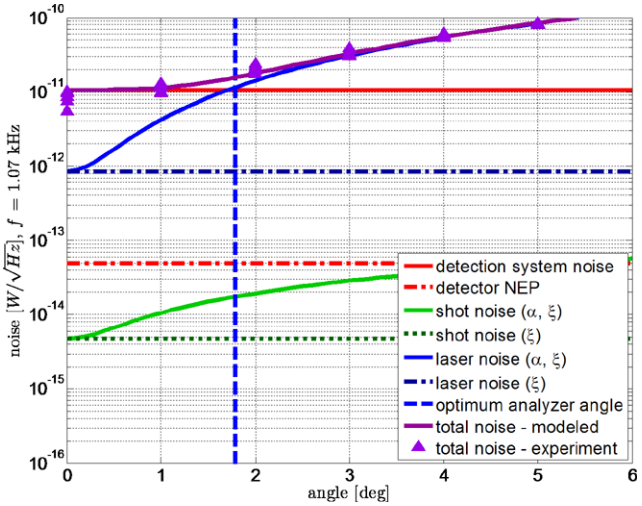

Fig. 3 Noise contributions for FRS-AC using the parameters B, C, D obtained in the fit of the experimental measurements, converted to power using the H transfer function. B is associated with detection system noise, C is associated with shot noise, and D is associated with laser source noise

Based on these assumptions the result of the fitting of the measured noise data, shown in Fig. 3, yielded $B = 11947$ (1.0×10^{-11} W/Hz$^{\frac{1}{2}}$) and $D = 1.23\times10^{7}$ (1.1×10^{-8} W/Hz$^{\frac{1}{2}}$). We took the noise definition as the standard deviation of data points in the wings of the absorption line (150 points were analyzed away from the absorption line center). Figure 3 shows the measurement data together with the fitted model. All noise contributions derived from the fitting are also shown in the plot. At small α, the noise is dominated by the detection noise. The asymptotic shot and laser noise behavior is due to the finite extinction ratio of the polarizers, and the limit as the angle goes to zero is shown on the same plot.

The fitting results can also be used to calculate the optimum analyzer angle (also given in [6]), solved by taking the derivative of the SNR expression with respect to α, setting the result to zero, and solving for α:

$$\alpha_{\mathrm{opt}} = \sqrt[4]{\left(\frac{B}{D}\right)^2 + \left(\frac{C\cdot\sqrt{\xi}}{D}\right)^2 + (\xi)^2} \tag{3}$$

For $C \ll D$ and $\xi \ll 1$, the optimum angle becomes $\alpha_{\mathrm{opt}} \approx \sqrt{\frac{B}{D}}$, so that the effective laser noise and the detection noise are equal at this angle. At larger analyzer angles, the laser noise dominates and rapidly approaches the value for total noise. For our system, the optimum analyzer offset angle is 1.8 degrees, calculated using (2) and parameters obtained from the fit in Fig. 3.

The total measured detection system noise was significantly larger than the detector NEP (noise equivalent power) specified by the manufacturer. We performed analysis in order to determine the amount of expected noise and excess noise. The specified NEP of the photodiode was $N_{\mathrm{NEP}} = 5 \times 10^{-14}$ W/Hz$^{\frac{1}{2}}$. The total expected effective input referred noise at $\alpha = 0°$ can be calculated as 1×10^{-12} W/Hz$^{\frac{1}{2}}$ (0.4 pA/Hz$^{\frac{1}{2}}$) based on data sheet specifications of the analog front-end components and the measured B, C, and D. The electronic noise without the detector connected and with zero magnetic field was 1.4 pA/Hz$^{\frac{1}{2}}$ at 1 kHz (an equivalent optical noise power of 3.4×10^{-12} W/Hz$^{\frac{1}{2}}$), effectively measuring the Johnson–Nyquist noise of the 1 MΩ transimpedance resistor plus any excess noise of the circuit itself. With the Si detector connected and the laser light blocked, the noise was 2.9 pA/Hz$^{\frac{1}{2}}$ (7×10^{-12} W/Hz$^{\frac{1}{2}}$ equivalent optical noise power) at the same conditions. These measurements indicate that there are additional sources of detection noise which are larger than the amplifier noise and detector NEP.

The experimental measurement of 7×10^{-12} W/Hz$^{\frac{1}{2}}$ at $\alpha = 0$ shown in Fig. 3 matches satisfactorily; however, we believe that the unaccounted noise arises from secondary effects such as EMI. The EMI may have several origins including (in order of importance): (1) electromagnetic pick-up in the wires between the detector and preamplifier (2) the high impedance preamplifier configuration, (3) ground loops, or (4) digital/analog power and ground plane crosstalk (processor, laser current/TEC driver, and analog front-end are integrated on the same board as compactly as possible).

Using the noise data, we can determine the effect of modifying the various sensor parameters to determine the best configuration of the sensor components. In the next few paragraphs, we explore these effects by varying the model parameters through simulation to determine possible optimizations.

A plot of the SNR as a function of the detection noise B is shown in Fig. 4a. It clearly demonstrates that reducing B increases the SNR. It also shows that with decreasing B, the optimum analyzer angle is decreasing to suppress the level of the laser noise at the detector and achieve $B = D$ at the optimum analyzer offset angle. This happens until the polarizer quality limits the system performance (shown as a plateau in the SNR vs. B curve).

A reduction of the laser noise D can provide even stronger enhancement of the system sensitivity. As shown in Fig. 4b, a decrease in D can result in $\sqrt{D}$ improvement in SNR. The smaller D allows uncrossing the analyzer (larger α_{opt}) until the lower laser noise becomes equal the detection noise level. Decreasing D will not result in a plateau related to the polarizer quality as observed in Fig. 4a for the B parameter. This is because the allowed laser power at the detector increases, diminishing the importance of the polarizer quality. However, at increased laser power, detector saturation effects may occur, which can limit the SNR. The simulation does not include this saturation effect, since it strongly varies between different detectors.

In the present system, the laser noise is 1.8 nW in 1-Hz bandwidth at 1.07 kHz when measured after the first polarizer and before the cell using 280 μW of total laser power. The laser operated at a bias current of 6 mA, including the threshold current of 3.5 mA. Assuming that laser current fluctuations are responsible for all laser amplitude noise, the relative laser noise $d = 6.3 \times 10^{-6}$ in 1-Hz bandwidth allows the calculation of the noise in the current driver. The light-current characteristics of the VCSEL used in this work can be considered linear in the region of operation with a laser slope efficiency of ~0.112 W/A. This allows estimating the effective absolute maximum current noise in our laser driver to be ~16 nA in 1 second (or 2.6 ppm relative current noise). Since a switching power supply generates our laser driver power rail, this level of current noise is relatively low, and further reduction will be challenging. Although improvements are possible in the electronic circuit architecture, we believe that the reduction of the laser noise should be focused primarily on the selection of a different laser chip with more appropriate characteristics such as low intrinsic noise level, and higher power (as will be discussed later in the text).

Figure 4c shows the effect of improving the extinction ratio of the polarizers. The simulation shows that the current system works in the detection noise limited regime in which the polarizer quality has minimal effect on SNR. In this regime, the implementation of more compact and lower quality polarizers can reduce the cost and the size of the optical system (e.g., wire grid polarizers instead of birefringent crystal). Reducing ξ by 10× would result in only 30% reduction of the current SNR. The polarizer quality becomes important when the laser noise at α_{opt} is comparable to the laser noise observed when $\alpha = 0$.

Figure 4d shows the modeled SNR as a function of input optical power to the sample cell. With input power of 280 μW, the signal-to-noise ratio was about 611 (for 21% O_2 in air). This analysis shows that with higher input power (given the relative laser noise d remains constant), we can improve SNR for the current system. With future applications in low power sensors (e.g., in distributed wireless sensor networks) this feature will provide opportunities to reduce power consumption when high precision is not needed, and switch to high power consumption when necessary (i.e., triggering the high-precision sensing based on anomalous events such as sensing of an oxygen depletion near a fire). With higher laser powers (and constant d) the system becomes laser noise dominated and requires operation at smaller α; thus, polarizer quality becomes important.

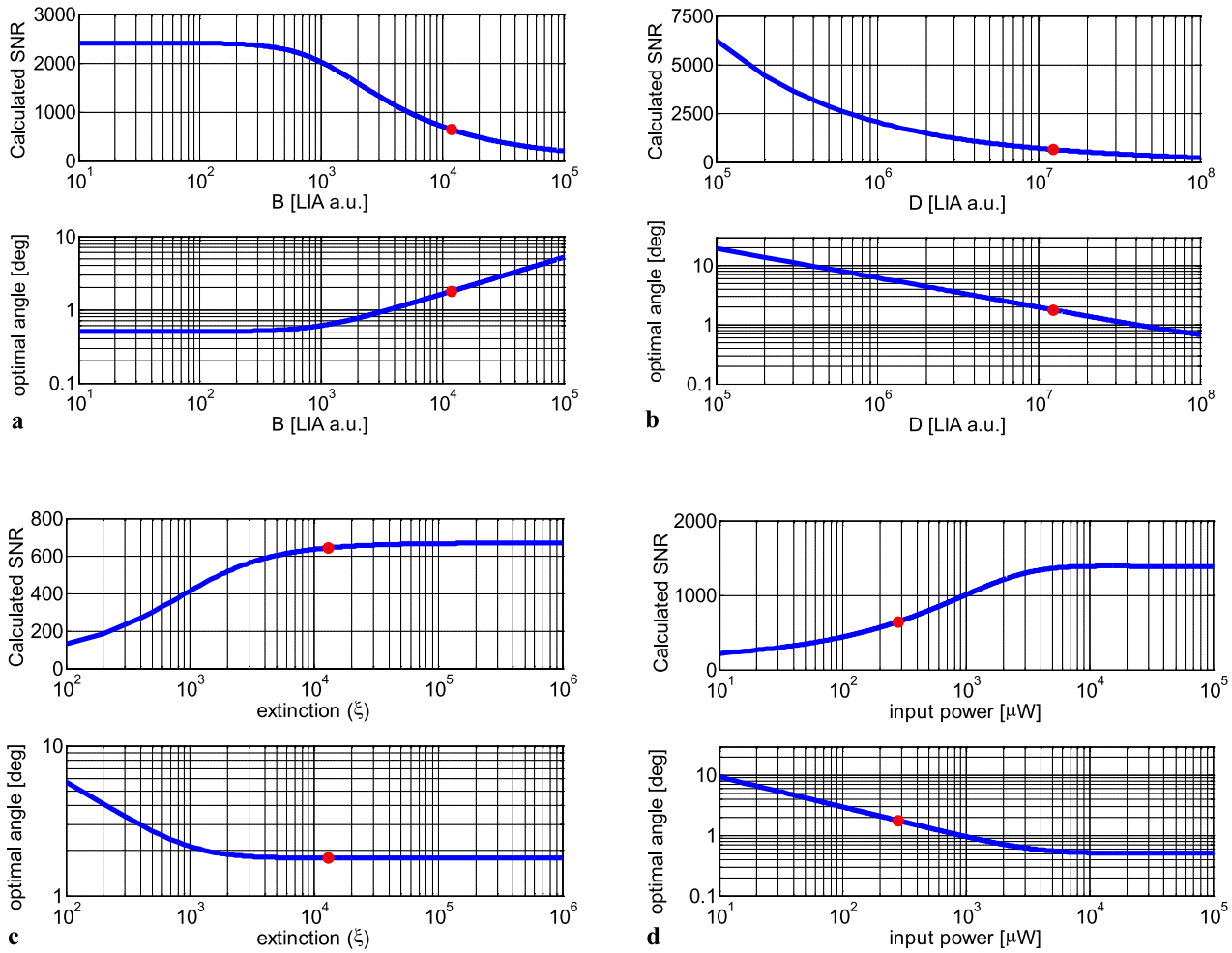

Fig. 4 **a** Calculated SNR vs. detection system noise (B parameter) at the optimum α_{opt}. The *red point* indicates the present system. The reduction of B by 10× would improve the SNR by 3×. **b** Calculated SNR vs. laser noise (D parameter) at the optimum α_{opt}. The reduction of D by 100× improves SNR by 10×, with an accelerating growth trend. **c** Calculated SNR and resulting optimum analyzer offset angle vs. extinction ratio for FRS-AC. **d** With a constant ratio of laser power noise to optical power (d parameter), increased optical power by 10× can provide ∼3× higher SNR

This is evident in Fig. 4d in which SNR reaches a plateau above 5 mW and optimum angle decreases. In this regime further increase of the laser power without improving other parameters of the system (e.g., polarizer quality) would not improve the sensitivity.

4.1.2 Spectral measurements

Figure 5a shows the FRS spectrum of ambient air oxygen 21% (by volume) at 225 Torr with 15-cm optical path. We set α at 2 degrees instead of the optimum 1.8 degrees due to limited angular resolution of the polarizer rotation stage (∼0.5 deg setting accuracy). We considered noise amplitude to be the standard deviation (1σ) of 150 points in the wings of the absorption line for the noise (shown in Fig. 5b) and the signal amplitude parameter A to be the maximum peak-to-trough signal observed in the full spectral scan for the signal. Lock-in basis rotation maximizes the FRS signal in the in-phase demodulated component for each individual spectrum. The EMI pickup (from the modulation of current in the magnetic coil) in the detection channel produces an offset in the signal. This offset was stable over time, and a simple offset baseline correction allows for its removal.

The asymmetry in the measured FRS spectral feature indicates that the intensity of RHCP and LHCP components are not perfectly balanced (elliptical polarization). As a result, we observe a signal associated with magnetic circular dichroism (MCD), which is related to selective absorption by the Zeeman split absorption line components (see Ref. [8]). As mentioned earlier, we observe dependence of the polarizer extinction ratio on the angular position of the gas cell located between the polarizers. This indicates that the cell windows influence the polarization of the laser radiation and deteriorate the linear polarization state, allowing

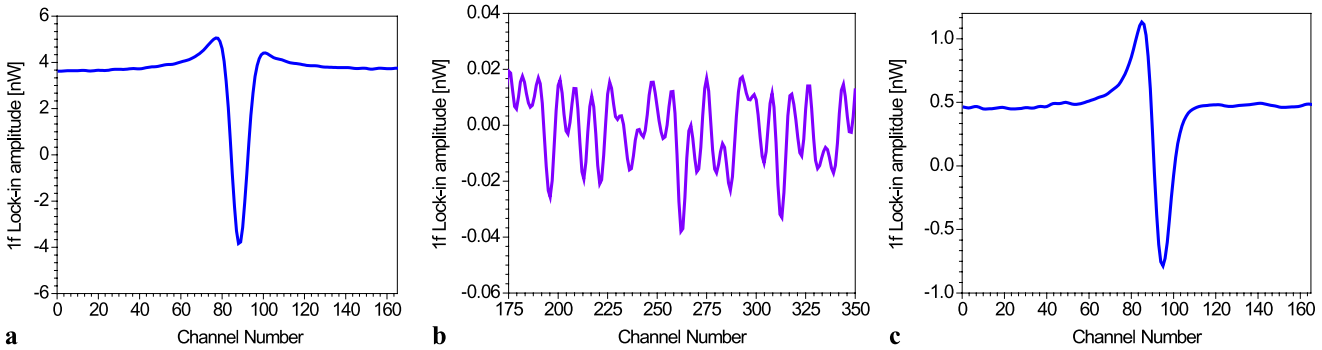

Fig. 5 **a** A Faraday rotation spectrum of the $^{P}P_1(1)$ line of oxygen measured for 21% O_2 in air at 225 Torr with SNR(1σ) = 611, 2° analyzer offset, and 0.54-Hz detection bandwidth. **b** Noise measured in the wings of the absorption line (channel numbers 175–350 in (**a**), with a linear baseline removal). **c** MCD signal produced by FRS-AC at $\alpha = 0°$

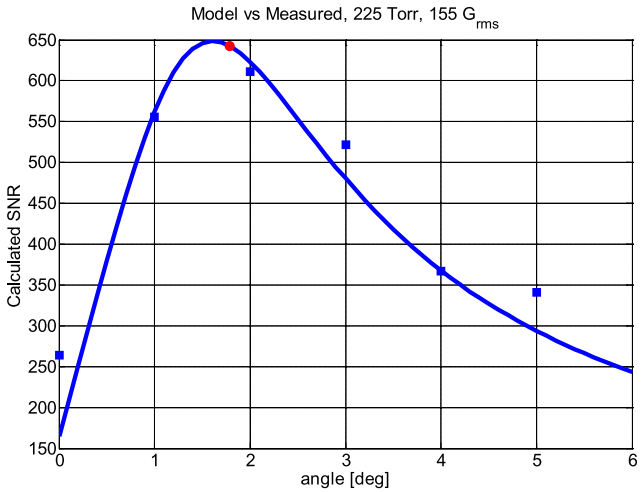

Fig. 6 The model calculated SNR (*line*) and the measured SNR (*points*) vs. analyzer angle. The calculated optimum angle is shown in red, neglecting dichroism

MCD effects. This effect can be clearly observable at $\alpha = 0°$ as shown in Fig. 5c. At this angle, the FRS signal is at a minimum, and the MCD of the gas sample causes the remaining intensity modulation.

To verify the optimization of system parameters, we performed measurements of the SNR as a function of analyzer offset angle. As shown in Fig. 5c, the MCD signal observed at 0° contributes to the total measured signal amplitude. Therefore, the model described by (2) we should first correct for the MCD effect before applying it to the data. We assume that the MCD signal component depends on optical power and follows:

$$S_{\mathrm{MCD}} = k \cdot P_0 \cdot \left(\alpha^2 + \xi\right) \tag{4}$$

where k can generally represent a spectrally dependent MCD signal. We use the MCD signal measured at $\alpha = 0°$ where $S_{\mathrm{MCD}} = k \cdot P_0 \cdot \xi$, and we correct the MCD contribution by subtracting the value calculated with (4) from the measured FRS signal at other analyzer offset angles α. The SNR model compared to corrected experimental data is shown in Fig. 6.

The calculated optimum angle should also account for the S_{MCD} term. However, for practical purposes, as long as S_{MCD} is much smaller than $A \cdot \alpha$ at the optimum α_{opt} (which is the case for our system with $\alpha_{\mathrm{opt}} = 1.8°$), we can use the calculation based on (3) with negligible impact on overall system performance.

SNR also depends on sample pressure. Therefore, we performed measurements at various sample pressures to identify the optimum operating conditions for the target sensor system. Since the operation at reduced pressures requires power-inefficient pumps with moving parts and other gas handling components, ideally the sensor should operate at atmospheric pressure. There are two processes that must be analyzed in order to fully characterize the pressure dependence of the FRS signal. First, the maximum FRS signal occurs when the Zeeman splitting is roughly equal to the full width of the target absorption line. Second, the peak absorbance and the resulting dispersion increase with increasing pressure of the sample (this is particularly evident at low pressures in the Doppler limited regime).

In the current system, the maximum magnetic flux density we could produce with the coil was 155 G_{RMS} (primarily due to Joule heating exceeding the thermal limit), which can provide only ~0.0198 cm^{-1} Zeeman splitting (full distance between the RHCP and LHCP dispersion components) of the $^{P}P_1(1)$ oxygen line. This defines the upper limit of the Zeeman splitting; thus, the available field is not sufficient to provide optimum splitting for the target transition which has a full Doppler width of 0.028 cm^{-1}. In this case, the increase of the operating sample pressure (when applying maximum B-field) will cause the two processes mentioned above to compete: (1) the pressure broadening of the line will cause decreasing FRS signal due to increasingly insufficient Zeeman splitting, and (2) the increasing peak absorbance and dispersion will cause an increase in the FRS

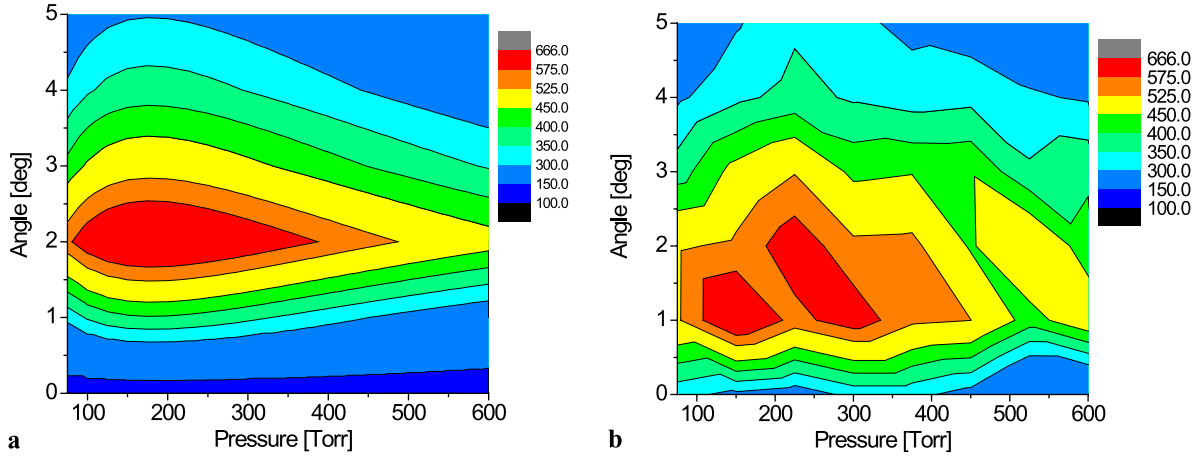

Fig. 7 Plots of simulated and experimental SNR vs. angle and pressure, at 155 Gauss RMS magnetic field. **a** Simulation based on the noise model parameters and FRS signal simulations. **b** SNR calculated from experimental data

signal. We simulate these effects using (2) where SNR is calculated based on our B, C, and D parameters and the FRS signal has been computed using refractive index calculations based on a Kramers–Kronig transformation of the HITRAN absorbance spectrum of O_2. The results of this simulation shown in Fig. 7a as an SNR optimization map (SNR as a function of α and sample pressure) clearly demonstrate that the best operating conditions occur within relatively broad limits around $\alpha = \sim 2°$ and pressure of ~180 Torr.

Figure 7b shows our experimental data acquired for the same conditions as those used in Fig. 7a simulation. This experimental SNR map shows a similar trend as observed in the simulation. The optimum operating analyzer offset angle is shifted towards smaller α with minimally increased SNR in comparison to the simulated value, which indicates that our fitting performed in Fig. 2 overestimated the B parameter. The observed maximum SNR of 611 measured for a 21% O_2 air mixture at 225 Torr, $\alpha = 2°$, and 0.52 Hz bandwidth indicates that the optical path and bandwidth normalized minimum detectable concentration (MDC) is 69.3 ppmv·m·$Hz^{-\frac{1}{2}}$. The optimization map indicates that higher magnetic fields are required to enable atmospheric pressure operation of the sensor.

All results presented above maximized the peak FRS signal within the in-phase component (X) of the lock-in, resulting in no signal in the orthogonal component (quadrature, Y). This provides ease of modeling and direct comparisons with the DC-method. This optimization method is effective only when all noise contributions are random. However, we suspect noise sources which are coherent with the modulation frequency due to EMI. Due to the unknown phase of the coherent noise, varying the detection phase and maximizing the SNR (as opposed to maximizing signal only) provides further optimization. The modeling cannot predict the noise structure in advance; thus, the lock-in should initially measure both X and Y components simultaneously; then the optimum lock-in basis is rotated for maximum SNR in the X channel.

We provide an optimization map similar to Fig. 7 using the maximum SNR basis rotation. The results are shown in Fig. 8. The reduced noise level in the X-channel mimics reduced laser noise. The reduced d allows for larger α, allowing more signal through the analyzer. The SNR improves with this optimization, although some of the absolute signal will be lost in the quadrature component. The modeling presented in the previous section predicts behavior of the pure FRS signals and noise levels but does not account for this unknown coherent noise contribution. Thus, each system requires independent optimization for the best sensing performance.

Using the above SNR-optimization, we obtained a maximum SNR of 1473 for atmospheric concentration of 21% O_2 in air over 15-cm optical path at pressure of 225 Torr, with magnetic field of 155 Gauss rms, and at $\alpha = 4°$. According to HITRAN, the peak fractional absorption is 9.4×10^{-4} at these conditions. This corresponds to an equivalent minimum detectable absorption (MDA) of 8.85×10^{-7} $Hz^{-\frac{1}{2}}$ and a detection limit of 30 ppmv·m·$Hz^{-\frac{1}{2}}$. Additionally, optimum Zeeman splitting of the absorption line at 225 Torr using a higher magnetic field of ~700 G_{RMS} should provide 2.5× larger FRS signals. FRS systems with modulated magnetic field show drift-free performance over integration periods of up to 1 hour as shown in Ref. [6], and similar performance is expected for the system discussed here. Different long-term performance is expected for DC-FRS systems, which will be discussed in the following section. These results indicate the benefits of using FRS in place of conventional absorption spectroscopy for enhancement of sensitivity to paramagnetic species.

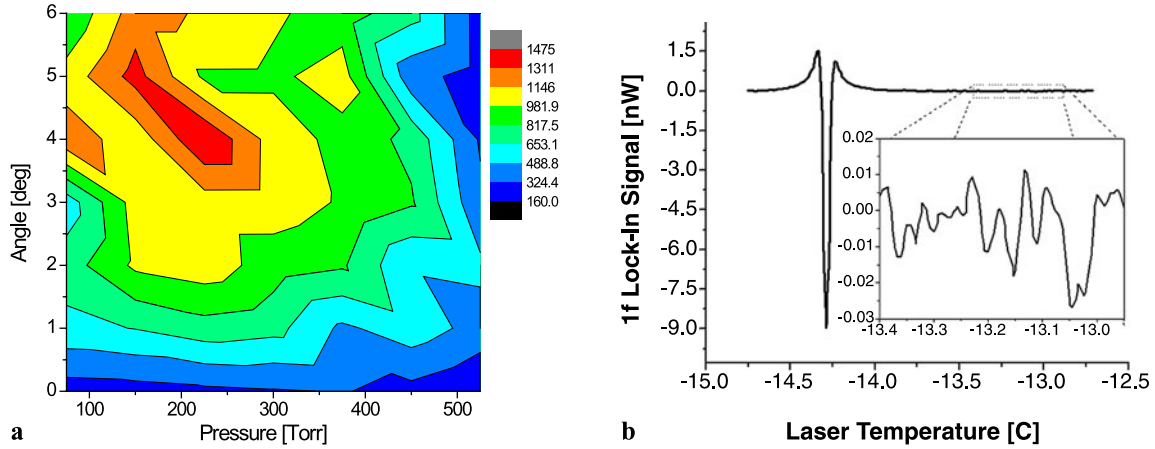

Fig. 8 **a** SNR after lock-in basis optimization measured as a function of sample pressure and analyzer offset angle at 155 Gauss RMS magnetic field. **b** A measured FRS spectrum of 21% O_2 in air with the maximum SNR = 1473 at 4° analyzer offset angle, and pressure of 225 Torr. The *inset* shows the noise in the spectral wings

4.2 DC field

We performed measurements using the static field in order to allow for future power consumption reduction and for increase of the available magnetic fields with permanent magnets. In the AC case, the power audio amplifier drives ∼30 W_{RMS} into the load impedance of the solenoid. This power consumption is too high for portable, handheld instrumentation, so a permanent magnet solution with equivalent static magnetic field would provide an ideal solution, allowing us to take advantage of FRS sensitivity enhancement combined with our ultra-low-power core sensing system demonstrated with TDLAS [9].

The static field FRS measurements of O_2 were previously performed and analyzed by Brecha et al. in Refs. [10, 11] using a diode laser. Here we investigate the DC-field approach by analyzing all noise sources present in the system and cross-compare with the AC case to determine suitability to quantitative trace gas sensing. In the DC-field approach, the FRS signal generation implements laser wavelength modulation by adding a sinusoidal modulation to the bias current of the laser chip. All measurements use equivalent conditions to the AC-field for direct comparison.

Figure 9 shows the spectral scan of the FRS-DC signal measured at first harmonic of the fundamental modulation frequency. The signal shape resembles the first derivative of the static difference in the dispersion spectral envelopes for LHCP and RHCP polarization components. The peak-to-peak amplitude of the FRS-DC signal is about half of the levels found in the FRS-AC case when the laser wavelength modulation depth is set to about ∼0.1 cm^{-1}.

Wavelength modulation allows all wavelength dependent spectral features (e.g., spectral fringes, absorption features, etc.) to contribute to the modulation of laser power. In the AC case, the effect generally does not exist, unless uncontrolled EMI produces laser wavelength modulation. The DC case is prone to this effect, which is proportional to the level of laser power arriving at the detector. In the FRS arrangement with a nearly crossed analyzer, the effect is strongly suppressed but still significant in comparison to FRS signal levels. Therefore the presence of parasitic etalon fringes and/or interfering spectral features impacts the performance of the system.

The noise observed in the wing of spectral feature showed in Fig. 7b is roughly twice the noise observed in the FRS-AC scan in Fig. 5. It is not immediately clear whether the etalon fringes are limiting the system performance. When we Fourier transform the noise data with the x-axis scaled in terms of optical cavity length, one can clearly identify a peak at a free spectral range of a ∼52-mm-long etalon. This corresponds to the optical length of the used Glan–Thompson polarizers (length 35 mm and $n = 1.48$). We verified that there are no air-spaced elements in our system which can produce such a free spectral range. Back calculating the fringe amplitude from the D parameter at 2° uncrossing with noise power 0.05 nW and the power hitting the detector 363 nW, we get a 1.3×10^{-4} fringe level, which is possible for an uncoated calcite prism with reflectance of 4% and angle of acceptance of 0–3 degrees from normal incidence.

The fringes appear as a structured baseline. Fringes have been ignored in the FRS literature but have a direct impact on the noise levels in the DC case. When the FRS SNR is maximized (through lock-in basis rotation) and modulation depth is set to ∼0.15 cm^{-1}, the fringe noise produces an SNR of 271 and causes MDA to lower to $4.8 \times 10^{-6}/\mathrm{Hz}^{\frac{1}{2}}$ with respect to $8.85 \times 10^{-7}/\mathrm{Hz}^{\frac{1}{2}}$ obtained in AC-field case. However, the MDA is still improved compared to 1.5 ×

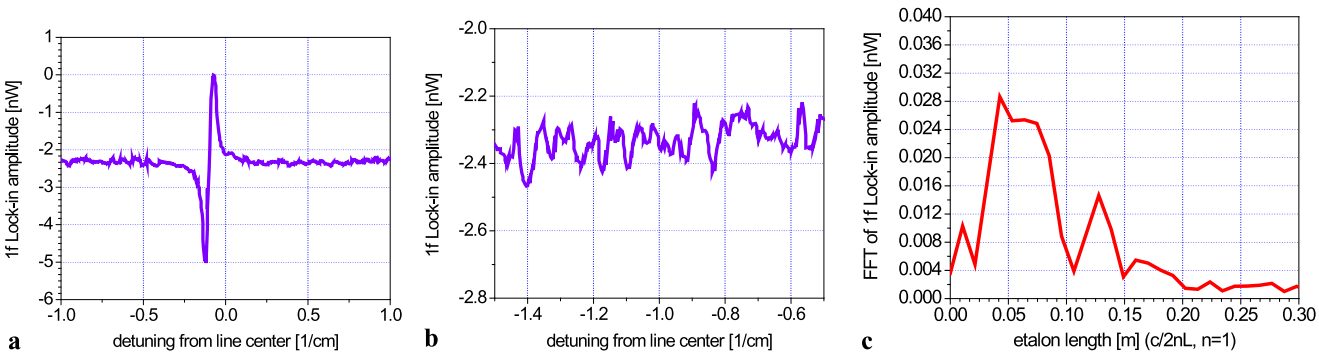

Fig. 9 **a** A FRS-DC-WM 1f spectrum of 21% of O_2 in the air at 225 Torr, modulation depth ∼0.1 cm^{-1} and analyzer angle at 2° for direct comparison with the FRS-AC model case. **b** The wings away from line center show slight sinusoidal structure, indicative of etalon fringes. **c** A Fourier transform of the data shows that the peak etalon length is ∼52 mm, which is the optical length of the polarizers

$10^{-5}/\mathrm{Hz}^{\frac{1}{2}}$ achieved using standard wavelength modulation spectroscopy with the same electronics and optical components (without the polarizer pair and gas cell which introduce etalons) [9]. Additionally, simulations show that optimum magnetic field in this DC case will provide 2.1× larger FRS signal power at the same pressure of 225 Torr. We also believe that the optical fringes limited performance will have significant impact on the long-term stability of the sensor. Thus, unlike the AC-FRS systems, the drift performance in DC-FRS should be comparable to conventional laser absorption spectroscopy showing Gaussian white random noise limited performance for ∼100 s (well optimized systems show ∼300-s maximum integration times [12]). Therefore, suppressing fringe noise is essential, and several approaches to obtain optical fringe suppression in DC-FRS are proposed below.

Appropriate selection of the modulation depth can further suppress the fringe noise; however, this will also affect the signal, which becomes more difficult to analyze. Therefore, the best and the most reliable methodology is to simply reduce fringes in the optical system by conventional means: using reflective optics (in place of transmission-based optical components), applying antireflection coatings, and careful alignment of the system.

We performed noise analysis similar to the AC-case. Our DC experimental data yielded $B = 8705$ and $D = 6.45 \times 10^7$, assuming C to be the same as the AC case. Detection noise B becomes slightly smaller due to the lack of AC magnetic fields causing EMI. The laser noise was measured as the standard deviation of the data points in the wing of the absorption line within the spectral scan, and therefore it also contains the contribution due to the fringe noise. Due to this effect, the D value in the DC case is larger than in the AC-field method. Figure 10 shows the overall noise in the system and all component noise sources present in the system.

The optimum angle decreases from 1.8° in the AC case to 0.8° in the DC field method, mainly to suppress the higher

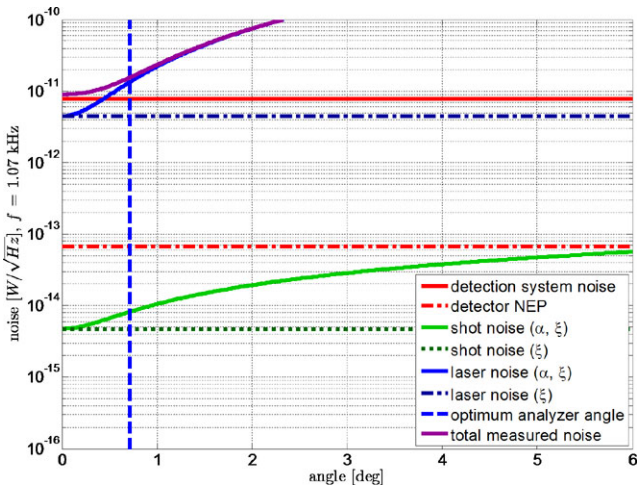

Fig. 10 Noise levels at optimum modulation depth maximizing the FRS signal (∼0.1 cm^{-1}). We used the same detector NEP and shot noise as the AC case

noise originating from the optical fringing, which is lumped into the laser noise component. Repositioning the polarizer pair off-axis can provide stronger fringe reduction; however, we anticipated direct comparison of both methods for exactly the same alignment conditions. Therefore, the AC and DC measurement differed only in magnetic drive method and wavelength control. In any case, alternate methods of fringe reduction in the future will allow us to reach higher stability and lower noise overall for the DC method.

Although the DC-field method appears five times less sensitive than the AC-field method when directly compared, the static magnetic field approach exhibits important characteristics that will lead to development of ultra-portable low-power field FRS sensor systems. Some potential capabilities and new design solutions are discussed in the following section.

5 Ultra low power FRS-DC sensing technology

The current table top prototype of the sensor system targets low-power spectroscopic sensing applications. Two major system components are responsible for nearly 100% power dissipation: (1) a vacuum pump (∼50 W) and (2) a magnetic field coil driver (∼30 W). Both components are undesirable for field applications since they introduce high power requirements, moving parts (in the case of the pump), waste Joule heating, and complexity to the system. Generally, spectroscopic sensors work at reduced pressure to minimize collision broadening of spectral features and improve specificity. In FRS, most of the potential interfering species such as H_2O and CO_2 are not magnetically active, and this physical mechanism provides the specificity. Therefore, use of pumping is primarily for improvement of the FRS signal due to the limitations in the available magnetic field, which is optimum when the Zeeman splitting matches the absorption line width. Thus, higher magnetic fields can provide Zeeman splitting sufficient for lines at atmospheric pressure (∼1500 G for the $^PP_1(1)$ line), and a vacuum system (including the gas cell and windows) will be optional. An open-path approach also effectively eliminates the problem of window birefringence. However, higher B field requires much stronger electromagnets, which in the AC field approach produces more severe EMI. Therefore, a DC-field approach which takes advantage of strong permanent magnets (e.g., based on rare earth elements such as Neodymium) provides a preferable solution for field deployable sensor systems.

In this work we focused on the $^PP_1(1)$ transition of oxygen which exhibits a greater g-factor than high-J transitions. Thus, this $^PP_1(1)$ transition is more suitable for measurements with lower magnetic fields. Based on our FRS signal modeling, the application of higher magnetic fields available from permanent rare earth magnets will remove the issue of lower g-factors, and stronger transitions with higher J numbers will produce larger FRS signals.

Based on the identified noise sources, there are several possible improvements for future versions of the FRS sensor systems. We may consider DFB diode lasers operating at the same wavelength for the spectroscopic source instead of the current VCSEL. Greater laser output power (∼10 mW) and reduced fractional laser noise d (with an assumption of the same performance of the laser driver and typical slope efficiency of 0.8 A/W) will provide 3–5× improvement in SNR. Furthermore, we will implement a differential measurement method with $\alpha = 45°$ FRS measurements employing a dual beam polarization prism as an analyzer (e.g., Wollaston, or Rochon prism) and a balanced detector [13]. This method eliminates the need for expensive high-quality polarizer pairs, high-sensitivity detectors, and shows higher immunity to deterioration of the linear polarization state. This will allow for application of multipass cells and suppression of the etalon fringes which are common mode in both polarization states for the DC case. The addition of a custom compact 3.5 meter multipass cell (which we developed previously [9]) will increase the optical path within the magnetic field (multipass FRS has also been explored in [14]). With a proper combination of the optimizations identified in this work, we expect the entire compact multipass FRS system to target 0.5 ppmv detection limits in less than 1 second, which would be useful in measuring CO_2–O_2 biotic exchange rates.

6 Conclusion

We explored the SNR performance of modulated and static magnetic fields for FRS and found that the signals should be relatively similar, but etalon related noise can dominate the static DC field with wavelength modulation case. We analyzed the optical power tradeoff for our system and showed that a 2-mW laser with the same fractional intensity noise would give 2× higher sensitivity for the current configuration. We also demonstrated that extinction ratio only improves performance asymptotically when various other noise sources are present. Finally, we identified targets for improvement of SNR in next generation low-power FRS system which can be used for scalable multinode distributed sensor network technology and handheld FRS based spectrometers.

Acknowledgements The authors would like to thank Prof. Mark Zondlo for a laser which could target the $^PP_1(1)$ line and Yin Wang for valuable discussions on Faraday Rotation. This work was sponsored in part by the National Science Foundation (NSF) Engineering Research Center Mid-Infrared Technologies for Health and the Environment (MIRTHE), the NSF Major Research Instrumentation award #0723190 for the openPHOTONS systems, and an innovation award from The Keller Center for Innovation in Engineering Education.

References

1. G. Litfin, C.R. Pollock, R.F. Curl, F.K. Tittel, J. Chem. Phys. **72**, 12 (1980)
2. openPHOTONS repository. www.openphotons.org
3. Alpha Omega Instruments, Oxygen Analyzer—Oxygen Sensor Types. http://aoi-corp.com/additional_information/oxygen_sensor_types/default.html
4. M. Laakso, M. Jalonen, S. Laukkanen, in *Proc. Technical Papers of ISA*, 2005
5. G. Di Stefano, Chem. Phys. Lett. **426**, 1 (2006)
6. R. Lewicki, J.H. Doty, R.F. Curl, F.K. Tittel, G. Wysocki, Proc. Natl. Acad. Sci. **106**, 31 (2009)
7. S.G. So, A. Amiri Sani, L. Zhong, F.K. Tittel, G. Wysocki, in *Proc. Workshop on Earth and Space Science Applications*, 2009
8. C.D. Boone, F.W. Dalby, I. Ozier, J. Chem. Phys. **113**, 19 (2000)

9. S. So, A.A. Sani, L. Zhong, F. Tittel, G. Wysocki, in *Proc. The 8th ACM/IEEE International Conference on Information Processing in Sensor Networks*, 2009
10. R.J. Brecha, L.M. Pedrotti, D. Krause, J. Opt. Soc. Am. B **14**, 8 (1997)
11. R. Brecha, L. Pedrotti, Opt. Express **5**, 5 (1999)
12. D. Richter, A. Fried, P. Weibring, Laser Photon. Rev. **3**, 4 (2009)
13. H. Adams, D. Reinert, P. Kalkert, W. Urban, Appl. Phys. B **34**, 4 (1984)
14. A. Hinz, D. Zeitz, W. Bohle, W. Urban, Appl. Phys. B **36**, 1 (1985)